PAPER

Check for updates

Synergistic engineering of poly(3-hydroxybutyrate) architecture and stereomicrostructure achieves enhanced material properties

Maëlle T. Gace, [ID] [a] Ethan C. Quinn, [ID] [a] Fateme Shariatikia, [ID] [b]
Jorge L. Olmedo-Martínez, [ID] [b] Shu Xu, [c] Alejandro J. Müller [ID] *[b,d] and
Eugene Y.-X. Chen [ID] *[a]

Chemically engineering the stereomicrostructures of biodegradable poly(3-hydroxybutyrate) (P3HB) has been shown to be an effective strategy to largely modulate its properties for mono-material product design, but whether coupling this method with P3HB architecture engineering could yield an even more effective strategy has yet to be demonstrated. Here, through stereochemically and architecturally controlled polymerization, four-arm star-shaped P3HBs consisting of stereo-perfect isotactic, iso-rich, and syndio-rich stereomicrostructures, as well as their linear counterparts of comparable molar mass as controls, have been synthesized. Comprehensive and comparative characterization studies have uncovered various degrees of impacts of the P3HB architecture on thermal transitions, crystallization behaviors, mechanical performance, and rheological and gas barrier properties. In particular, coupling both stereomicrostructure and architecture engineering approaches has produced synergistically enhanced effects on the overall material properties, providing a more powerful strategy to design mono-materials with vastly different properties without changing their chemical composition.

Introduction

Over the past century and a half, the development of synthetic polymers from petroleum byproducts has revolutionized industries by providing cost-effective, durable, and high-performance plastics.[1–7] Despite their essential role in society, the prevailing approach for designing and producing plastics has followed a linear economy model, often failing to address sustainable end-of-life options.[8,9] The urgent challenge we now face is to find sustainable alternatives to petroleum-based, nondegradable plastics to mitigate the global plastics crisis. One promising approach involves synthesizing biobased and biodegradable plastics.[10–14]

Polyhydroxyalkanoates (PHAs) – a class of natural polyesters produced by bacteria and other microorganisms – emerge as a promising solution to address this demand for biobased plastics. Renowned for their ability to degrade under managed and unmanaged conditions, alongside their tunable thermal and mechanical properties, PHAs present an attractive alternative to petroleum-based commodity plastics.[15–22] Among PHAs, biologically produced, isotactic P3HB (*it*-P3HB$_b$) exhibits perfect isotacticity with an absolute (*R*)-stereoconfiguration and is a highly crystalline material with a high melting temperature (T_m) of ~175 °C. It shows good barrier properties and high tensile strength, but it is highly brittle (an elongation at break (ε_B) of ~3–5%) and possesses a narrow processing window (due to its low decomposition temperature (T_d) of ~250 °C).[17,23,24] Despite significant advancements in engineering PHA metabolic pathways, the biosynthetic route remains constrained by microstructural and architectural complexity limitations.[25–29]

Since the 1960s, significant research has focused on the ring-opening polymerization (ROP) of lactones to create synthetic analogs of *it*-P3HB$_b$.[30] The simplest monomer for producing P3HB is the highly strained, four-membered β-butyrolactone (BBL). Although BBL has been extensively studied, achieving highly isotactic to perfectly isotactic P3HB materials remains challenging. Historically, polymerizations of a *racemic* mixture of BBL have shown limited success, yielding polymers with a P_m (probability of *meso*-linkages between monomer units) of ≤0.92.[31–40] This limitation arises from the

[a]Department of Chemistry, Colorado State University, Fort Collins, CO 80523-1872, USA. E-mail: eugene.chen@colostate.edu
[b]POLYMAT and Department of Polymers and Advanced Materials: Physics, Chemistry and Technology, Faculty of Chemistry, University of the Basque Country UPV/EHU, Donostia-San Sebastián 20018, Spain. E-mail: alejandrojesus.muller@ehu.es
[c]Applied Materials Division, Argonne National Laboratory, Lemont, IL 60439, USA
[d]IKERBASQUE, Basque Foundation for Science, Plaza Euskadi 5, Bilbao 48009, Spain

small, flat monomer structure and the polymerization pathways involving both alkyl and acyl cleavages, which impairs the ability to achieve high control and isotacticity or utilize less stereoselective catalysts.[17,41,42] Recently, studies have demonstrated that lowering the temperature to 0 °C or even to −35 °C or using enantiopure catalysts can increase isoselectivity.[40,43,44] Seeking an alternative route, we developed a method to synthetically produce isotactic P3HBs (*it*-P3HBs) with $P_m > 0.99$ by employing the ROP of the *racemic* eight-membered dimethyl diolide (*rac*-8DL^{Me}) with C_2-chiral salen-based metal complexes.[45]

The 8DL^{Me} platform was then extended in efforts to enhance the toughness of *it*-P3HB through a range of strategies. These efforts included copolymerizing *rac*-8DL^{Me} with 8DL^R (R = Et, ^{n}Bu, Bn) or other lactones,[46–51] engineering its stereomicrostructure,[52] implementing blending strategies,[53] exploring block architectures,[46,54] alternating *it*-PHAs,[55] and designing α,α-disubstituted PHAs.[56] Consequently, a diverse array of PHA materials emerged, spanning from strong yet brittle thermoplastics to ductile and tough thermoplastics and elastomers. It should be pointed out that, although the copolymerization approaches successfully toughened *it*-P3HB, they increase the synthetic and chemical complexity, complicating possible mechanical and chemical recycling routes and hampering the possibility of creating mono-material products.[57]

Commercial plastic products typically require multiple materials to function and adhere to common application standards, particularly in packaging.[57–59] However, recycling these multi-layer products is challenging and energy-intensive due to their immiscibility and/or different chemical compositions. These significant issues contribute to the rising demand for single-monomer-sourced mono-material product design as a more sustainable approach. Utilizing the stereomicrostructural engineering approach makes it possible to produce customized properties from a single monomer.[52]

Another method central to this study involves the engineering of P3HB's architecture. It has been shown that the physical properties of polymers can be modulated through architectural engineering, providing a means to achieve desired properties.[60–62] Recent developments in architectural engineering have allowed for synthesizing increasingly intricate polymer architectures, including star-shaped polymers. Star-shaped polymers are characterized by branched structures with multiple (>2) linear chains linked to a central point called the "core". Their simplicity in architectural deviation from linear polymers, higher-order architecture, and well-defined three-dimensional structure make them promising for designing and accessing advanced materials across diverse sectors such as electronics, medicine, and cosmetics.[63–65] The branching of star polymers reduces polymer entanglement compared to their linear equivalents, distinguished by their compact structure and packing in the molten phase.[66–69] Furthermore, other advantages include enhanced ultimate stress and toughness due to more pronounced strain hardening and superior strain recovery.[70,71] Consequently, these advanced polymeric architectures hold significant promise for improving the processability of P3HB.

Although star architectures have been implemented in the ROP of various lactones and derivatives,[72] reports detailing the synthesis of P3HB star homopolymers remain scarce. In 2015, Mehrkhodavandi and coworkers reported the synthesis of three- and six-armed star-shaped P3HBs through the ROP of BBL using indium and zinc catalysts.[73] The resulting P3HBs are atactic to syndio-rich, with P_r (probability of *racemic* linkages between monomer units) values ranging between 0.55 and 0.62. Their study explored the effects of branching, highlighting improved packing of segments within a single chain. Additionally, Du and coworkers successfully generated multi-arm star-shaped P3HB from bio-based polyols through zinc-catalyzed ROP of BBL to produce atactic P3HB.[74] Nevertheless, the performance properties of such materials are compromised by the limitations of stereocontrol. Thus, there remains a need for achieving star-shaped P3HB polymers with enhanced tacticity as well as for investigating potential impacts of P3HB stereomicrostructures, when coupled with architectural variations, on their material properties.

Here, we report the synthesis and comprehensive characterization of 4-armed star-shaped P3HBs *via* ROP of 8DL^{Me} with a tetra-ol initiator for architectural control and yttrium catalysts for stereomicrostructural control. In this work, we showed that coupling architectural engineering with stereomicrostructural engineering can more effectively modulate the nucleation and crystallization ability of P3HB to improve the thermal, mechanical, and barrier properties of the resulting P3HB materials, as well as reduce their melt viscosities. The results highlight the potential of architectural manipulation to generate a diverse set of material properties for mono-material products.

Experimental details

Materials

All syntheses and manipulations of air- and moisture-sensitive chemicals and materials were carried out in flame-dried Schlenk-type glassware with a dual-manifold Schlenk line or in an inert gas (N$_2$)-filled glovebox. HPLC-grade organic solvents were first sparged extensively with nitrogen during filling of 20 L solvent reservoirs and then dried by passage through activated alumina, followed by passage through Q-5-supported copper catalyst (for toluene and hexanes) stainless steel columns. HPLC-grade dichloromethane (DCM) was stirred overnight over CaH$_2$ under N$_2$ and distilled under N$_2$ before use.

Yttrium chloride YCl$_3$ was purchased from Sigma-Aldrich Chemical Co. and used as received. Benzyl alcohol (BnOH) was purchased from Alfa Aesar, purified by stirring over CaH$_2$ overnight, distilled, and then stored in the glovebox over activated Davison 4 Å molecular sieves. N,N,N',N'-tetrakis(2 hydroxyethyl)ethylenediamine was purchased from Sigma-Aldrich Chemical Co., purified by stirring over CaH$_2$ overnight, vacuum-distilled, and then stored in the glovebox. Dimethyl 1,4-dibenzyl-2,5-dioxocyclohexane-1,4-dicarboxylate was purchased from ThermoScientific and used as received. Iodomethane was purchased from Oakwood Chemical and

used as received. The oxidant 3-chloroperoxybenzoic acid (mCPBA, ≤77%) was purchased from Sigma Aldrich and used as received. The literature procedures were employed for the preparation of rac- and $meso$-8DL^{Me}, which was sublimated twice before use for polymerizations.[45] Yttrium precursor, Y[N (SiHMe$_2$)$_2$]$_3$(THF)$_2$, and the yttrium complexes were synthesized according to reported procedures.[45,75,76]

Biological P3HB (it-P3HB$_b$) was purchased from Sigma-Aldrich (M_w (weight-average molar mass) = 437 kDa). Isotactic polypropylene (it-PP, 5 mm granules) (M_n (number-average molar mass) = 97.0 kDa) was purchased from Sigma-Aldrich. Low-density polyethylene (LDPE, 3–4 mm granules, melt flow index (MFI) = 7.5, Product Code INEOS LDPE 19N430) was purchased from INEOS Olefins & Polymers Europe. High-density polyethylene (HDPE, 2–4 mm granules, MFI = 7.6, Product Code ET32-GL-000110) was purchased from Goodfellow. Polybutylene adipate terephthalate (PBAT, M_w = 88.5 kDa) was purchased from BASF (Ecoflex F Blend C1200). All polymers were used as received.

General polymerization procedures

Polymerizations were performed in 7.0 mL glass reactors inside an inert N$_2$ glovebox at ambient temperature (∼25 °C). The reactor was charged with a predetermined amount of monomer (8DL^{Me}) and solvent (DCM) in the glovebox, and a mixture of catalyst and initiator in solvent was stirred at ambient temperature for ∼10 min in another reactor. The polymerization was initiated by the rapid addition of the catalyst solution to the monomer solution. After the desired time, 0.01 mL of an aliquot was taken from the reaction mixture and quenched with a 5% solution of benzoic acid in CDCl$_3$ for ^{1}H-NMR analysis to obtain the percent monomer conversion data. The polymerization was then immediately quenched by the addition of ∼5 mL of HCl/MeOH (5% solution). The quenched mixture was then precipitated into an excess amount of cold methanol while stirring, filtered, washed with cold methanol to remove any unreacted monomer, and dried in a vacuum oven at 60 °C overnight to a constant weight. Larger-scale reactions were performed in the same way but using a 50 mL glass reactor.

Instrumentation

Absolute molar mass measurements. Measurements of polymer absolute M_w, M_n, and dispersity ($Đ = M_w/M_n$) were performed via size exclusion chromatography (SEC). The SEC instrument consisted of an Agilent HPLC system equipped with one guard column and two PLgel 5 μm mixed-C gel permeation columns and coupled with a Wyatt DAWN HELEOS II multi (18)-angle light scattering detector and a Wyatt Optilab TrEX dRI detector; the analysis was performed at 40 °C using chloroform as the eluent at a flow rate of 1.0 mL min^{-1}, using Wyatt ASTRA 7.1.2 molecular weight characterization software. Samples were run using the "assume 100% mass recovery option" which calculated dn/dc internally based on a precisely known polymer concentration of the sample prior to injection, which was 2.00–4.00 mg mL^{-1}.

Spectroscopic characterization. NMR spectra were recorded on a Bruker AV-III 400 MHz spectrometer (400 MHz, ^{1}H; 100 MHz, ^{13}C) at 25 °C. Chemical shifts (δ) are reported in ppm with the solvent resonance employed as the internal standard (chloroform-d_1 at 7.26 ppm for ^{1}H NMR and 77.0 ppm for ^{13}C NMR).

Thermal analysis. Melting transition temperature (T_m), crystallization temperature (T_c), glass transition temperature (T_g), and heat of fusion (ΔH_f) were measured by differential scanning calorimetry (DSC) on an Auto Q20, TA Instruments. All T_m and T_g values were obtained from a second scan unless noted otherwise. Both heating and cooling rates were 10 °C min^{-1}. Decomposition temperatures ($T_{d,5\%}$ defined by the temperature at 5% weight loss) and maximum rate decomposition temperatures (T_{max}) of the polymers were measured by thermogravimetric analysis (TGA) on a Q50 TGA Analyzer, TA Instruments. Polymer samples were heated from ambient temperatures to 700 °C under N$_2$ at a heating rate of 10 °C min^{-1}. Values of T_{max} were obtained from derivative (wt%/°C) $vs.$ temperature (°C) plots [derivative thermogravimetry (DTG)], while T_d values were obtained from wt% $vs.$ temperature (°C) plots.

Mechanical analysis. Tensile stress/strain testing was performed by an Instron 5966 universal testing system (10 kN load cell) on dog-bone-shaped test specimens (ASTM D638 standard; Type V) prepared via compression molding using a Carver Auto Series Plus Laboratory Press (Carver, Model 3889.1PL1000, Max Force 15 ton) equipped with a two-column hydraulic unit (Carver, Model 3912, maximum force 24 000 psi). Isolated polymer materials were loaded between non-stick Teflon paper sheets into a stainless-steel mold with inset dimensions of 30 × 73.5 × 0.87 mm, prepared in-house, and compressed between two 6″ × 6″ steel electrically heated platens (EHPs) at a set pressure of 3000 psi and at each material's respective T_m. Specimens for analysis were generated via compression molding and cut using an ASTM D638-5-IMP cutting die (Qualitest) to standard dimensions. Mechanical behavior was averaged for all the specimens measured for each individual species investigated. The thickness (0.38 ± 0.01 mm), width (3.18 mm), and grip length (26.4 ± 0.2 mm) of the measured dog-bone specimens were measured for normalization of data using Bluehill Universal Software (TA). Test specimens were affixed to the screw-tight grip frame. Tensile stress and strain were measured to the point of material failure at a grip extension speed of 5.0 mm min^{-1} under ambient conditions. Young's modulus (E, MPa), stress at break or ultimate strength (σ_B, MPa), and elongation at break (ε_B, %) are obtained from the software analysis. Toughness values (U_T; MJ m^{-3}) were obtained by the manual calculation (integration) of the area under the stress/strain curve.

The detailed tensile testing results of commercially available HDPE, LDPE, it-PP, and PBAT (individual stress/strain curves and tables) were previously reported, and the values were taken from those papers.[77,78] Film processing (melt compression molding) was performed as previously indicated ($vide$ $supra$). LDPE samples were heated to 110 °C. HDPE samples

were heated to 150 °C. *it*-PP samples were heated to 175 °C. PBAT samples were heated to 135 °C. Tensile stress/strain tests were performed as previously indicated (*vide supra*).

Rheological analysis. Rotational shear rheology experiments were performed on a Discovery Series Hybrid 2 (DHR-2) rheometer (TA Instruments) in flow-sweep testing mode with a shear rate range of 10^{-3}–10^{3} (s^{-1}). Test specimens were trimmed at predetermined temperatures above T_m. The polymer material was loaded between two 8 mm steel parallel-plate EHP geometries under an N$_2$ (30 psi) gas flow and allowed to equilibrate at the specified temperatures for a minimum of 30 s. Rheometer control and data analysis were performed using TA Instruments TRIOS software.

Polarized light optical microscopy analysis. A polarized light optical microscope, Olympus BX51 (Olympus, Tokyo, Japan), equipped with an Olympus SC50 digital camera and with a Linkam-15 TP-91 hot stage (Linkam, Tadworth, U.K.; coupled to a liquid nitrogen cooling system) was used to observe the morphology of the samples after crystallization from the melt. Films with around 100 μm thickness were prepared by melting the samples between two glass slides. The samples were heated to 190 °C or 135 °C to erase their thermal history, maintained at this temperature for 1 min, and then cooled from the melt at 20 °C min^{-1} to 25 °C.

Successive self-nucleation and annealing (SSA). SSA is a thermal fractionation technique that is performed using a Differential Scanning Calorimetry (DSC) to study the different molecular segregation capacities that, normally, the semi-crystalline polymeric systems exhibit during isothermal crystallization and annealing processes. The SSA experiments were carried out following the protocol defined by Müller *et al.*[52] The first heating scan is the one in which the thermal history of the sample is erased (heating the sample 20 °C above the melting point and maintaining it at this temperature for 3 minutes). In this work, during the second step, the samples were cooled down at 20 °C min^{-1} to −30 °C. After 1 min at this temperature, the sample is heated at the same rate to a temperature 7.5 °C lower than the end-temperature melting (as a proxy for the ideal self-nucleation temperature)[52] and held for 3 min at that temperature (T_s). Subsequently, the sample was cooled again to −20 °C and held at this temperature for 1 min. This cyclic process was repeated by varying the T_s values 10 times, decreasing it at each cycle by 7.5 °C. Finally, the sample was heated to the molten state (200 °C in this case) to observe the results of the SSA thermal fractionation. All the scans were performed at 20 °C min^{-1} using a PerkinElmer DSC 8000 with an Intracooler II as the cooling system. This equipment was calibrated using indium and tin as standards.

Water vapor transmission rate (WVTR). WVTR was measured using a modified version of ASTM E96/E96M-16 (2016).[79] Standard 10 mL gas chromatography vials (Agilent Technologies, Santa Clara, CA) were used, each containing 7 mL of DI water. The film circles were sandwiched between two rubber sealing washers with outer and inner diameters of 20 mm and 9 mm, respectively. They were then placed on the vial openings and sealed using standard GC vial aluminum caps of 9 mm in diameter. Water vapor could only diffuse through the exposed circular area of the film. The sealed vials were then placed in an HPP 260 environmentally controlled oven (Memmert USA, Eagle, WI, USA) at 23 °C and 50% relative humidity for 24 h to allow water absorption and achieve a steady diffusion state. After the conditioning period, the initial mass of each vial was measured, followed by 5 additional mass measurements over the next 120 h. Mass loss was plotted as a function of time, and the WVTR was determined from the slope of the obtained curve. All reported values are the average of 3 replicates. To obtain the water vapor permeability (WVP), the permeance was multiplied by the film thickness. The permeance was calculated by dividing the WVTR by the water vapor pressure difference (ΔP) across the film. ΔP was determined based on the saturation vapor pressure of water at the test temperature (2812 Pa at 25 °C) and the relative humidity difference (50%).

Results and discussion

Synthesis of *it*-, *ir*-, and *sr*-star-shaped P3HB

This study employed monomers, *rac*-8DL^{Me} and *meso*-8DL^{Me},[45,52,54] initiators, benzyl alcohol (BnOH) as the monoinitiator (I_a) for linear P3HB synthesis and *N,N,N′,N′*-tetrakis(2-hydroxyethyl)ethylenediamine as the tetra-functional initiator (I_b) for star-shaped P3HB synthesis due to its good solubility in dichloromethane (DCM), and pre-catalysts, yttrium salen complexes, were chosen for their steric openness and selectivity towards 8DL^{Me}.[45] Along with monomer and catalyst choices, the ratio between the catalyst and initiator is also important for achieving efficient polymerization. In the case of the tetra-functional I_b, a 4 : 1 [Y] to [I_b] ratio is necessary to generate the corresponding four-armed yttrium alkoxide active propagating species *via* instantaneous alcoholysis of the yttrium complex.

At the outset of this work, we showed that the initiation occurred at all four initiating sites of I_b, rather than at mono-, di-, or tri-initiation sites. Specifically, when pre-catalyst complex **1** was reacted with initiator I_b in different ratios (1 : 1, 2 : 1, 3 : 1, and 4 : 1), ^{1}H-NMR showed that the intensity of the methylene peak next to the alcohol group, –CH_2-OH, decreased as the ratio was gradually increased and became unmeasurable when the ratio reached 4 : 1 (Fig. S1), suggesting the formation of the active yttrium alkoxide species on each arm of the initiator. As simultaneous propagation of each of the four-armed alkoxide species is critical to generate discrete star-shaped P3HB, kinetic experiments were performed to interrogate the reactions of *rac*-8DL^{Me} with **1**/I_b and **1**/I_a in *rac*-8DL^{Me}/catalyst/initiator ratios of 400 : 4 : 1 and 400 : 1 : 1. Since there are four propagation sites in the case of the **1**/I_b system for the star-P3HB synthesis, we observed its polymerization occurred faster than the **1**/I_a system for the comparative linear P3HB synthesis, approximately by a factor of four, as evidenced by the slopes of the kinetic plots of the polymerization reactions: 0.22 for the linear polymer synthesis *versus* 0.83 for the star

polymer synthesis (Fig. S2), all while maintaining low dispersity (*Đ*), pointing to that all four initiating sites propagated similarly.

The selection of catalyst allowed us to adjust the stereoselectivity of the polymerizations to achieve stereodiverse star-shaped P3HBs with medium to high molar masses (M_n = 32.3 to 208 kg mol^{-1}). Thus, upon optimization of the reaction conditions, the ROP at a [*rac*-8DL^{Me}]/[**1**]/[**I$_b$**] ratio of 600:4:1 at room temperature (RT, ~25 °C) achieved >99% monomer conversion in 10 min, affording high molar-mass isotactic four-armed star-shaped P3HB (*it-s4*-P3HB) with a low *Đ* (M_n = 204 kg mol^{-1}, *Đ* = 1.15; Table 1, Run 1). Incorporating bulky trityl (CPh$_3$) groups at the 3-position of the salcy ligand framework leads to remarkable stereocontrol with P_m > 0.99 and [*mm*] (*meso*-triads or isotacticity) > 99%, as shown by {^{1}H} ^{13}C NMR spectra where only one peak in each stereochemistry-

diagnostic (methyl, methylene, and carbonyl) region was found (Fig. S3 and S4). To the best of our knowledge, this is the first report of highly isotactic star-P3HB. Of note is the distinctive aspect of this polymerization system, which relies on employing a racemic catalyst (**1**, Fig. 1). Upon mixing **I$_b$** and racemic **1**, a total of 16 possible diastereomers of the propagating alkoxy catalyst could be generated from the instantaneous alcoholysis. Despite this complexity, thanks to the exclusive enantioselectivity of the catalyst, that is, (*R,R*)-**1** selectively polymerizes (*S,S*)-8DL^{Me} while (*S,S*)-**1** selectively polymerizes (*R,R*)-8DL^{Me},[45] the ensuing polymerization produced quantitatively stereoregular *it*-P3HB. To further confirm the stereoselectivity outcome of this system, enantiopure (*R,R*)-**1** was also utilized in the ROP of *rac*-8DL^{Me} with **I$_b$** (Table 1, Run 4; Scheme S1). This polymerization achieved 50% conversion due to its exclusive selectivity to only polymerize (*S,S*)-8DL^{Me}, consistent with

Table 1 Selected results of the [Y]-catalyzed ROP of 8DL^{Me} with mono- and tetra-functional initiators[a]

Run	[M]	Cat.	[I]	Term	[M]/[cat]/[I]	Time (min)	Conv. (%)	M_n[d] (kg mol^{-1})	*Đ*[d] (M_w/M_n)	T_m[e] (°C)	ΔH_f[f] (J g^{-1})	X_c[g] (%)	R_g[d] (nm)	P_m[h]	$T_{d,5\%}$[i] (°C)	T_{max}[i] (°C)
1	*rac*-8DL^{Me}	**1**	**I$_b$**	*it-s4*-P3HB	600/4/1	10	>99	204	1.15	168	71.2	48.8	22.1	>0.99	254	281
2	*rac*-8DL^{Me}	**1**	**I$_a$**	*it-l*-P3HB	800/1/0.25	15	>99	208	1.01	171	87.8	60.1	68.7	>0.99	247	280
3	*rac*-8DL^{Me}	**1**	**I$_a$**	*it-l*-P3HB (arm)	200/1/1[b]	30	>99	32.3	1.07	160	77.5	53.1	n.d.	>0.99	233	262
4	*rac*-8DL^{Me}	(*R,R*)-**1**	**I$_b$**	(*S,S*)-*it-s4*-P3HB	400/4/1[c]	5	50	162	1.15	164/174[f]	79.6	54.5	36.9	>0.99	263	284
5	*rac*-8DL^{Me}	**2**	**I$_b$**	*ir-s4*-P3HB	1000/4/1	90	>99	200	1.23	105[f]	24.7	16.9	31.3	0.91	244	280
6	*rac*-8DL^{Me}	**2**	**I$_a$**	*ir-l*-P3HB	750/1/0.25	60	71	232	1.25	106[f]	44.0	30.1	78.0	0.91	258	287
7	*rac*-8DL^{Me}	**2**	**I$_a$**	*ir-l*-P3HB (arm)	250/1/1[b]	15	>99	59.0	1.04	118[f]	47.8	32.7	n.d.	0.91	262	291
8	*meso*-8DL^{Me}	**2**	**I$_b$**	*sr-s4*-P3HB	750/4/1	10	>99	146	1.27	123	21.4	14.7	42.2	0.21	239	264
9	*meso*-8DL^{Me}	**2**	**I$_a$**	*sr-l*-P3HB	800/1/0.5	35	>99	139	1.19	125	30.8	21.1	87.7	0.21	246	274
10	*meso*-8DL^{Me}	**2**	**I$_a$**	*sr-l*-P3HB (arm)	150/1/1[b]	15	>99	42.0	1.18	130	14.5	9.93	60.1	0.21	251	282

[a] Conditions: 8DL^{Me} = 1.25 g (7.26 mmol) in DCM (7.26 mL), 1.0 M, ~25 °C, except for runs 3, 4, 7, and 10. [b] Conditions for runs 3, 7, and 10: 8DL^{Me} = 650 mg (3.76 mmol) in DCM (3.76 mL), 1.0 M, ~25 °C. [c] Conditions for run 4: 8DL^{Me} = 100 mg (0.58 mmol) in DCM (0.39 mL), 1.5 M, ~25 °C. [d] Determined by size exclusion chromatography (SEC) coupled with a Wyatt DAWN HELEOS II multi (18) angle light scattering detector and a Wyatt Optilab TrEX dRI detector and performed at 40 °C in chloroform. [e] Determined by DSC (10 °C min^{-1}) from second heating scans. [f] Determined by DSC (10 °C min^{-1}) from first heating scans. [g] See SI Note 2. [h] Calculated from the ^{13}C NMR spectrum (CDCl$_3$, 23 °C). [i] Values obtained using thermogravimetric analysis (TGA) at a heating rate of 10 °C min^{-1}. n.d. = not determined.
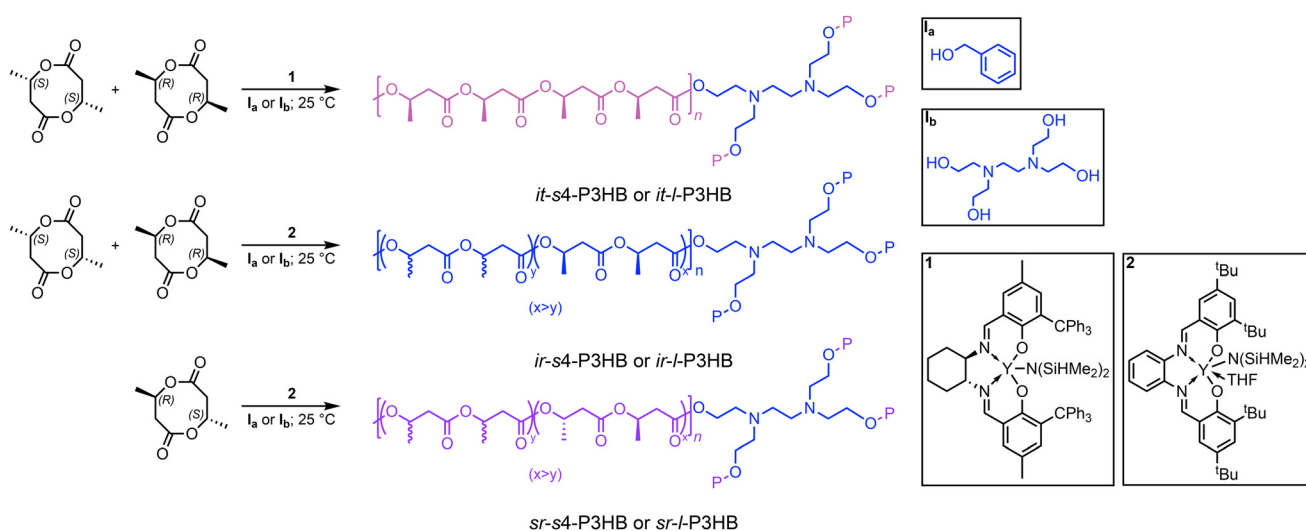

Fig. 1 Overall reaction schemes for the synthesis of linear and star-shaped *it*-P3HB, *ir*-P3HB, and *sr*-P3HB.

previous findings.[45] Moreover, the resulting enantiopure star-P3HB exhibited perfect isotacticity, as confirmed by {^{1}H} ^{13}C NMR (Fig. S7).

Next, we synthesized iso-rich and syndiorich 4-armed star-shaped P3HBs, *ir-s*4-P3HB and *sr-s*4-P3HB, using $\mathbf{I_b}$ and achiral pre-catalyst **2**. Specifically, *ir-s*4-P3HB was synthesized through the ROP of *rac*-8DL^{Me} (Table 1, Run 5; Fig. 1), while *sr-s*4-P3HB was synthesized in the same manner through the ROP of *meso*-8DL^{Me} (Table 1, Run 8; Fig. 1). The ROP reactions were optimized at a [*rac*-8DL^{Me}]/[**2**]/[$\mathbf{I_b}$] ratio of 1000 : 4 : 1 (Table 1, Run 5) and a [*meso*-8DLMe]/[**2**]/[$\mathbf{I_b}$] ratio of 750 : 4 : 1 (Table 1, Run 8) at RT, achieving >99% monomer conversion in 90 and 10 min, respectively. These polymerizations yielded high molar-mass *ir-s*4-P3HB (M_n = 200 kg mol^{-1}, Đ = 1.23) and *sr-s*4-P3HB (M_n = 146 kg mol^{-1}, Đ = 1.27). The stereomicrostructures of *ir-s*4-P3HB and *sr-s*4-P3HB were confirmed by {^{1}H} ^{13}C NMR analysis (Fig. S8–S13), showing [*mm*] (82%) and [*mr*] (18%) triad sequences with a P_m value of 0.91, and [*rr*] (58%) and [*mr*] (42%) triad sequences with a P_r value of 0.79, respectively.

Thermal properties and crystallization behavior

DSC revealed a T_m of 168 °C for *it-s*4-P3HB, similar to the T_m of 171 °C observed for its linear counterpart (Table 1, Runs 1 and 2, Fig. S14 and S15). This high T_m renders it desirable for high-performance applications, resembling the characteristics observed for *it*-PP. It is noteworthy to highlight that the crystallinity of *it-s*4-P3HB appeared lowered by 11.3% in comparison with its linear counterpart (X_c = 60.1% determined by the degree of crystallinity; Table 1, Run 2) with a chain length approximately corresponding to the four arms, a phenomenon attributed to the polymer's slower crystallization.[60] Moreover, maintaining similar degradation temperatures to the linear analog, with a T_d of 254 °C and T_{max} of 281 °C, indicates that implementing architectural engineering does not compromise the thermal properties. However, *it*-P3HB has a higher T_m and a relatively low T_d that is only about 80 °C above its T_m, posing challenges for melt-processing due to its narrow processing window (difference between T_d and T_m).[17]

Installing a controlled amount of stereo-defects into the backbone of the polymer can effectively reduce their crystallinity and T_m values.[52,53,80] Thus, *ir-s*4-P3HB (Table 1, Run 5) exhibits a lower T_m of 105 °C only observed in the 1st heating scan, accompanied by a lower degree of crystallinity (X_c = 16.9%). With a similar T_d of 244 °C, *ir-s*4-P3HB exhibits a broader processing window of 139 °C compared to only 76 °C for *it-l*-P3HB (Table 1, Run 2). These results showed that the principles learned through our recent work on *sr*- and *ir*-P3HB can be readily applied here.[52,53] We postulated that the stereo-errors found in *ir-s*4-P3HB are randomly incorporated along the chain, interrupting the crystallization of the linear stereo-regular chain segments and thereby lowering both T_m and heat of fusion (ΔH_f). Likewise, *sr-s*4-P3HB exhibits a T_m of 123 °C, a ΔH_f = 21.4 J g^{-1}, and a T_d of 239 °C, which broadens the processing window up to 116 °C. Notably, both of these star polymers exhibit a lower degree of crystallinity compared

to their linear counterparts (16.9% *vs.* 30.1% for *ir*-polymers and 14.7% *vs.* 21.1% for *sr*-polymers).

To better understand the crystallizability differences between linear and star-shaped P3HBs, successive self-nucleation and annealing (SSA) thermal fractionation studies were performed on all three-star polymers and their linear analogs for comparison purposes.[81–84] Fig. 2 shows the final DSC heating scans after applying the SSA protocol described in the Experimental Details section. Fig. 2A reveals *it*-P3HB polymers with the following differences: linear *it*-P3HB with a high M_n value (comparable to the M_n value of the *it-s*4-P3HB 4-arm star); linear *it*-P3HB with a lower M_n value (comparable to the M_n value of one of the arms of *it-s*4-P3HB, denoted as (arm)); and star *it-s*4-P3HB. These isotactic polymers were only slightly fractionated by SSA, meaning that only a few fractions are produced with a dominant large melting enthalpy fraction, where most of the material melts in the range of 160–180 °C. The highest M_n *it-l*-P3HB sample exhibited, as expected, the highest high-temperature melting fraction after SSA. In general, the low-temperature fractions are very small and broad.[85] The fractionated profile of the *it-s*4-P3HB sample is peculiar as it contains a small but high-temperature melting fraction (at ∼174 °C), even though this is the sample with the lowest degree of crystallinity from those reported in Table 1, attributable to its star topology.

Stars have arms radiating from a common center group of atoms that do not enter the crystal lattice and are segregated into the amorphous regions. On the other hand, stars tend to have their arms in a more stretched-out conformation, which allows them to interdigitate with neighboring star chains. We postulate that this effect causes this high-temperature melting peak fraction. This result could also indicate that star chains have a high level of interpenetration between them that could enhance percolation and, thus, mechanical properties, as explored in subsequent sections. As all the samples in Fig. 2A are highly isotactic ([*mm*] > 99%, see Table 1), the origin of the scarce SSA thermal fractionation can be ascribed mainly to their molar mass distribution and the intermolecular interactions present in these polymers. For the syndio-rich (*sr*) linear samples and the 4-arm sample in Fig. 2B, a much higher number of better-defined SSA thermal fractions were observed in comparison with the isotactic materials (Fig. 2A). It should also be noted that the melting range of the syndio-rich P3HB materials is lower in comparison with that of the isotactic materials. This increased capability of undergoing thermal fractionation in these syndio-rich materials is due to the much higher number of stereodefects that interrupt the linear crystallizable syndiotactic sequences along the chains ([*rr*] = 58%, [*mr*] = 42%, P_r = 0.79).[86] The stereo-defects also decrease the T_m of the material, as these defects limit the lamellar thickness that the polymer can achieve.

A similar result was obtained for *ir*-P3HB polymers (Fig. 2C), where a greater number of thermal fractions were observed in comparison with the *it*-P3HB samples, but fewer than in the *sr*-materials. It should be noted that the T_m range for the *ir*-P3HB materials is lower than that of the *sr*-P3HB
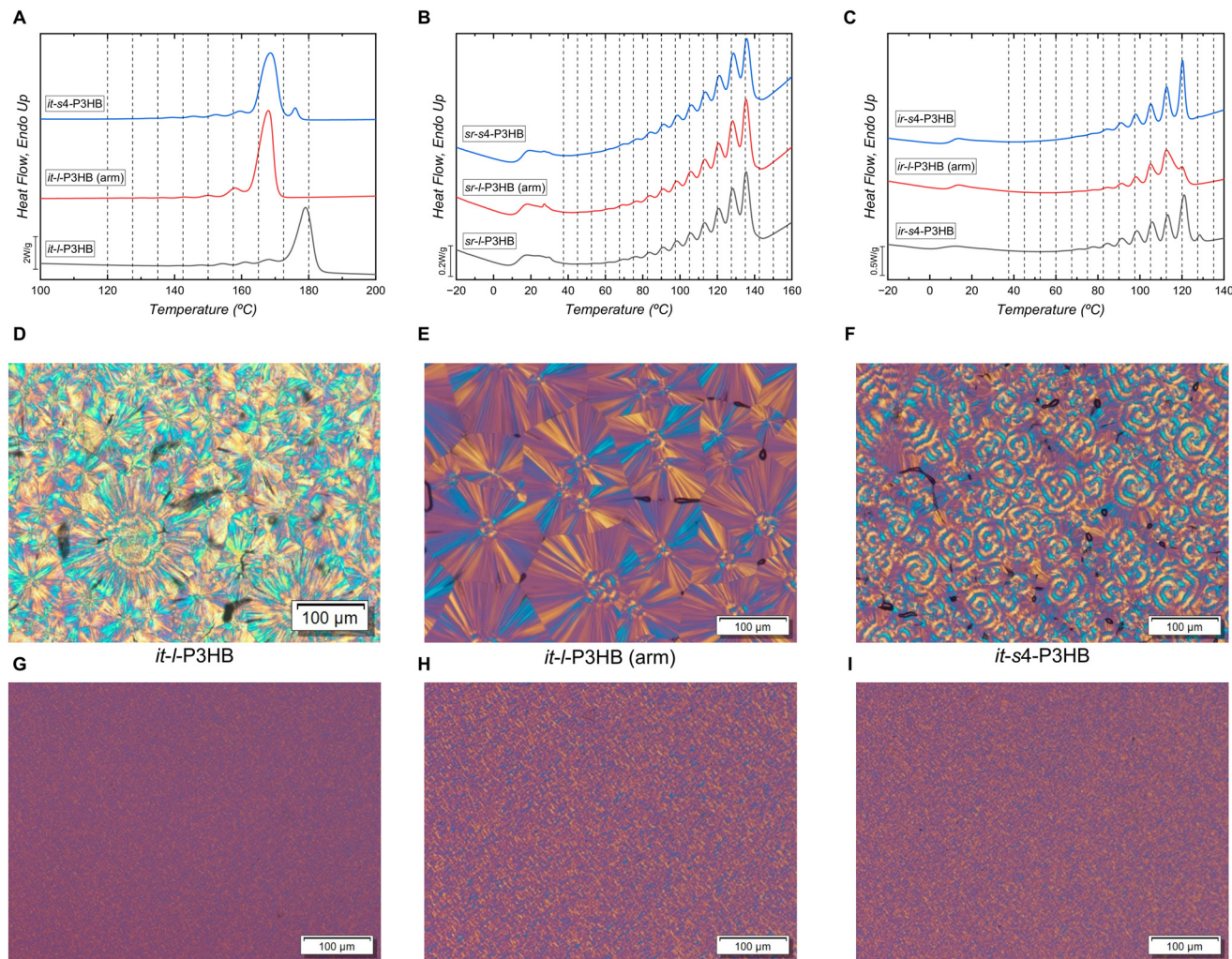
Fig. 2 Final DSC heating scans after SSA thermal fractionation (A–C) and PLOM micrographs (D–I) of *it*-P3HB (*it*-s4-P3HB, *it*-l-P3HB, and *it*-l-P3HB (arm)) and *sr*-P3HB (*sr*-s4-P3HB, *sr*-l-P3HB, and *sr*-l-P3HB (arm)). The (arm) denotes the lower molar mass linear P3HB with a chain length equivalent to one arm of star-shaped P3HB.

samples. Although *ir*-P3HB polymers contain fewer stereodefects along the chain ([*mr*] (18%) for *ir*-P3HB and (48%) for *sr*-P3HB), they appear less crystalline, as evidenced by the T_m observed only in the first heating scan. This difference is not due to a greater number of stereodefects but rather is attributed to the inherent crystallinity differences of the [*mm*] and [*rr*] triads. Specifically, [*rr*] triads tend to form thicker, more crystalline lamellae that require higher melting temperatures, whereas [*mm*] triads produce less crystalline structures with thinner lamellae, resulting in lower T_m and crystallinity. In fact, the quality of thermal fractionation, which refers to the degree of separation of each fraction (*i.e.*, if each melting peak is well separated from its neighbors by having the valleys of the endothermic signals approaching the baseline to a higher degree), is also higher in the iso-rich materials.

Fig. 2, panels D–I, presents the PLOM micrographs for the different P3HB samples studied here. All the samples underwent the same thermal treatment (heated to 190 °C or 135 °C and then cooled to 25 °C at a cooling ramp of 20 °C min⁻¹), and the images were taken after 12 h at 25 °C. All *it*-P3HB samples exhibit large spherulites due to the low intrinsic nucleation density of *it*-P3HBs. Specifically, *it*-l-P3HB is characterized by the formation of large spherulites, as shown in Fig. 2D and previously reported in the literature for bacterial and synthetic P3HB.[53] Reducing its M_n value produces, under the same thermal treatment, an increase in the spherulitic size and different optical properties. The micrographs in Fig. 2E show the dominant positive character of the linear low-M_n P3HB (*it*-l-P3HB (arm)) spherulites, consistent with previous reports of positive P3HB spherulites for similar materials.[86] On the other hand, the higher-M_n sample (*it*-l-P3HB, Fig. 2D) exhibits a more mixed negative/positive character. The *it*-s4-P3HB shows slightly smaller average spherulitic size and double-banded spherulites (Fig. 2F). Banding has been attributed to lamellar twisting as the lamellae grow radially inside the spherulites among other possibilities.[87–89] It has also been

reported that the spacing between bands tends to decrease with supercooling in the case of isothermal crystallization, but it can vary under non-isothermal conditions (*i.e.*, cooling rates).[86] Therefore, P3HB may or may not show banding, depending on the thermal history and molar mass. On the other hand, *sr*-P3HB polymers are characterized by forming many small-sized spherulites, as observed in Fig. 2 panels G–I. Stereodefects can increase the nucleation density of P3HB, as we have shown previously.[52,53] The spherulitic size is small but visible under the PLOM; hence, it should correspond to about 0.5 microns or larger. Finally, in the case of *ir*-P3HB polymers, no crystals were detected by PLOM, indicating that the spherulitic size must be smaller than the wavelength of light (400 nm) (Fig. S60–S62). The above results showed that star-shaped P3HBs exhibit a lower degree of crystallinity, smaller spherulites, and broader processing windows than their linear counterparts, making them well-suited for applications that demand enhanced thermal processability and controllable crystallinity.

Mechanical properties

To test the hypothesis that combining stereo-defects with the modulation of architecture in star P3HB materials would lead to superior mechanical performance when compared to their linear counterparts, we investigated their mechanical properties and compared them to their linear analogs of comparable molar mass, with representative stress–strain curves plotted in Fig. 3. Consistent with prior findings,[52,53] introducing stereo-defects into the stereo-perfect *it*-P3HB backbone

significantly enhances the mechanical performance of P3HB: while linear and star-shaped *it*-P3HB materials are brittle (Fig. 3A), the addition of stereo-errors produces ductile P3HB materials that exhibit a yield point, neck formation, and strain propagation until breakage (Fig. 3B and C).

Across all three (*it*-, *ir*-, and *sr*-) P3HB sets, the star-shaped P3HBs consistently exhibited noticeably higher ultimate stress (σ_B) and elongation at break (ε_B) values than their linear counterparts, indicating an overall improvement in mechanical properties conferred by the star architecture (Table 2). In the case of *it*-P3HB, differences between the star and linear P3HB materials were minimal, though the star P3HB still showed marginally higher σ_B ($\sigma_B = 34 \pm 0.6$ *vs.* 29 ± 3 MPa) and slightly improved ε_B ($\varepsilon_B = 4 \pm 0.3\%$ *vs.* $2 \pm 0.2\%$) *vs.* its linear counterpart (Tables S2, S3 and Fig. S47, S48). Despite these differences, both materials remained brittle (Fig. 3A). More substantial improvements were observed in the ductile P3HB materials containing stereo-defects. More specifically, *ir-s4*-P3HB (Fig. 3B) showed a high ε_B ($\varepsilon_B = 603 \pm 36\%$), a Young's modulus ($E$) of 566 ± 27 MPa, a σ_B of 23 ± 1 MPa, and a toughness (U_T) of 83 ± 8 MJ m^{-3}, noticeably superior to its linear analog of comparable molar mass and arm molar mass (Tables S4–S6 and Fig. S49–S52). A similar trend was observed for *sr-s4*-P3HB (Fig. 3C and Tables S7–S9, Fig. S53–S56), where the star P3HB outperformed the linear analog in σ_B ($\sigma_B = 35 \pm 0.4$ *vs.* 29 ± 2 MPa) and toughness ($U_T = 113 \pm 7$ *vs.* 84 ± 7 MJ m^{-3}). The percent changes in Table S12 quantify the relative differences between the star and linear polymers, with most properties exhibiting statistically significant increases for the
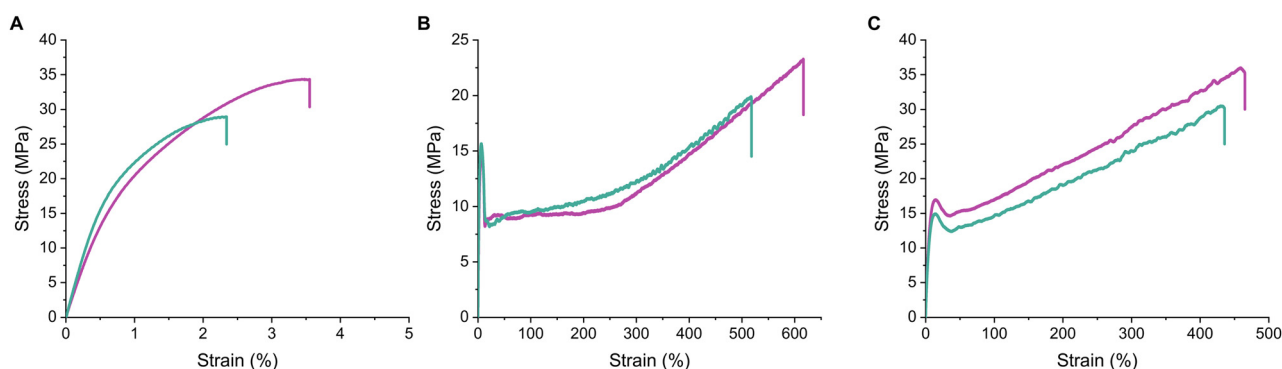

Fig. 3 Tensile stress−strain plots of star-shaped P3HB (magenta) and linear P3HB (cyan curves): (A) *it-s4*-P3HB (magenta) and *it-l*-P3HB (cyan) overlays of representative stress−strain curves; (B) *ir-s4*-P3HB (magenta) and *ir-l*-P3HB (cyan) overlays of representative stress−strain curves; (C) *sr-s4*-P3HB (magenta) and *sr-l*-P3HB (cyan) overlays of representative stress−strain curves.

Table 2 Stress−strain data for Fig. 3

Polymer name	σ_B (MPa)	ε_B (%)	σ_Y (MPa)	ε_Y (%)	E (MPa)	U_T (MJ m^{-3})
it-l-P3HB	29 ± 3	2 ± 0.2	—	—	3670 ± 179	0.4 ± 0.1
it-s4-P3HB	34 ± 0.6	4 ± 0.3	—	—	2933 ± 171	0.9 ± 0.1
ir-l-P3HB	19 ± 1	419 ± 25	15 ± 1	6 ± 0.4	715 ± 63	61 ± 7
ir-s4-P3HB	23 ± 1	603 ± 36	15 ± 1	7 ± 0.3	566 ± 27	83 ± 8
sr-l-P3HB	29 ± 2	419 ± 25	15 ± 0.2	14 ± 0.1	339 ± 4.9	84 ± 7
sr-s4-P3HB	35 ± 0.4	487 ± 33	16 ± 0.8	14 ± 0.1	349 ± 12	113 ± 7

star polymers. A difference was considered meaningful when it exceeded the combined experimental uncertainty, calculated as described in the SI (eqn (S1) and (S2); SI Note 1).

Increasing the number of arms in the star architecture from four to eight (*i.e.*, 8-arm *sr*-P3HB) can further enhance tensile properties compared to 4-arm P3HB, as detailed in the SI (Scheme S2, Tables S1, S10, S11 and Fig. S57–S59). This improved performance could be attributed to the 8-arm structure that promotes more efficient stress distribution and energy dissipation under tensile stress. Unlike linear chains, which rely on entanglement density for mechanical strength, the branched architecture of star-shaped polymers distributes stress more uniformly, reducing localized stress points that can lead to fracture. The improved mechanical performance likely arises from multiple factors: decreased crystallinity allows enhanced ductility, and the core of the star structure acts as a permanent covalent crosslink, contributing to improved stiffness by distributing stress more evenly and preventing crack propagation under applied loads. These results are also related to those obtained in the PLOM micrographs, since all the *it*-P3HB materials with large spherulites (50–100 mm) are brittle. Such brittleness arises from a high degree of crystallinity and acute stress concentration in the interspherulitic regions, promoting fragility and early fracture propagation.[53,90,91] Reducing the size of the spherulites by more than two orders of magnitude (below 0.5 μm) is a decisive factor, together with the reduction in crystallinity, to substantially improve mechanical properties and produce highly ductile materials.

The tensile properties of these three star-shaped P3HB materials were compared in Fig. 4 to common commodity plastics, including HDPE, *it*-PP, and PBAT. While *it*-*s*4-P3HB is a brittle material, its stress at break (σ_B) is comparable to the yield stress (σ_Y) of *it*-PP. On the other hand, *ir*-*s*4-P3HB offers significantly higher ductility, and *sr*-*s*4-P3HB

outperforms all the compared commodity plastics in overall mechanical performance, although its σ_Y is lower than that of HDPE and *it*-PP.

Rheological properties

The challenges associated with melt-processing *it*-P3HB are well-documented, primarily attributed to its high T_m and low T_d, paired with high viscosity at high molar mass, requiring high temperatures and/or high shear rates to process. Here, the branching structure plays a critical role in reducing polymer entanglement, potentially offering processing advantages over their linear equivalents. When compared to their linear analogues, star-shaped polymers have a smaller hydrodynamic volume and radius of gyration (R_g), as shown in Table 1, reflecting a more compact intramolecular packing within a single chain. This characteristic, coupled with reduced shear viscosity, contributes to improved melt processability. Thus, a lower shear viscosity η would be observed for star polymers due to reduced entanglement density and improved chain alignment between polymer chains at moderate to high shear rates, resulting in earlier and/or more pronounced shear thinning behavior.

Accordingly, the rheological properties of the synthesized polymers were studied *via* rotational shear rheology at 1 Hz at +10 °C of the T_m of the studied polymer (115 °C for *ir*-P3HB and 135 °C for *sr*-P3HB). For the *ir*-P3HB, the star polymer, *ir*-*s*4-P3HB, showed a much lower initial melt viscosity (η_0^*) value of 3106 Pa·s than that of the linear analog, 10 772 Pa·s (Fig. 5A). A similar trend was observed for *sr*-P3HB: 1080 Pa·s for *sr*-*s*4-P3HB *vs.* 3877 Pa·s for the linear analog (Fig. 5B). Apart from the differences in melt viscosity, their shear rate-dependent behavior also differs. The star polymers exhibit a broader Newtonian plateau at low shear rates, which corresponds to a region where viscosity remains nearly constant despite changes in shear rate. In this regime, the polymer chains have sufficient time to relax between shear deformations so that the material behaves like a Newtonian fluid and its viscosity is independent of shear rate. In contrast, at higher shear rates, polymer chains begin to align in the direction of flow and cannot fully relax between deformations, which leads to shear thinning, where viscosity decreases as shear rate increases. Once shear thinning begins, the viscosity of the star polymers decreases much more rapidly than that of the linear analogs (Fig. 5A and B). This more pronounced shear thinning for the star P3HB suggests that at the high shear rates typically encountered in processing methods such as extrusion or injection molding, star polymers are more likely to flow and exhibit stronger shear thinning effects, making them more processable than linear analogs.

Barrier properties

The synergistic coupling of high elastic modulus, high crystallinity, and excellent barrier properties establishes *it*-P3HB$_b$ as a compelling choice serving as a barrier layer in multi-layer packaging films.[24] To investigate the potential impact of the P3HB architecture on its barriers towards gas permeation, the
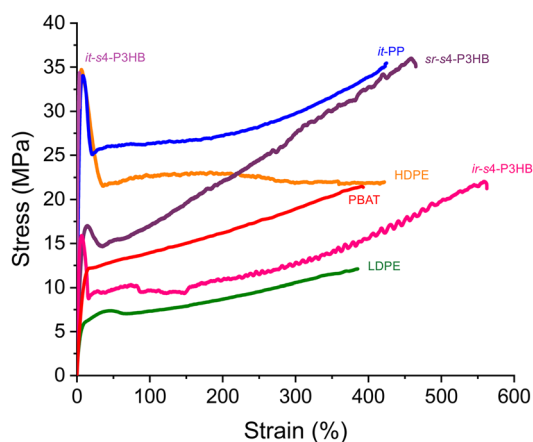

Fig. 4 Stress–strain curve overlays of *it*-*s*4-P3HB, *ir*-*s*4-P3HB, and *sr*-*s*4-P3HB with commodity plastics, including *it*-PP (blue), HDPE (orange), PBAT (red), and LDPE (green). Strain rate: 5.0 mm min^{-1}, ambient temperature.
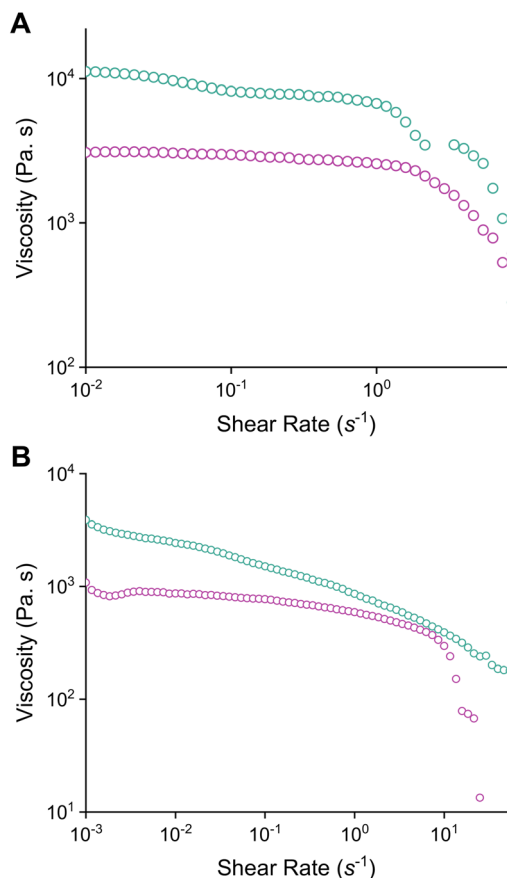
Fig. 5 Rheological properties of star-shaped P3HB (magenta) and linear P3HB (cyan curves): (A) *ir-s*4-P3HB (magenta) and *ir-l*-P3HB (cyan) overlays of rotational shear rheology curves; (B) *sr-s*4-P3HB (magenta) and *sr-l*-P3HB (cyan) overlays of rotational shear rheology curves.
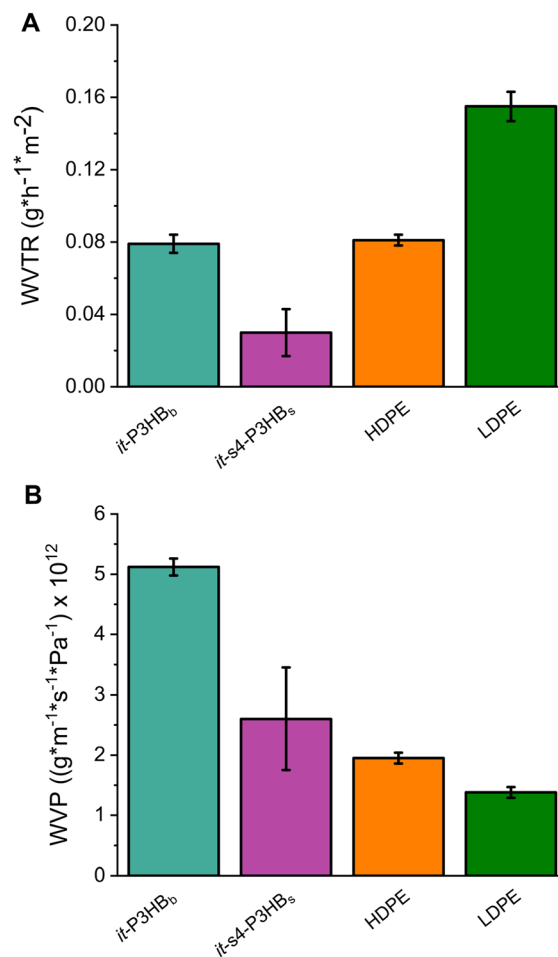

Fig. 6 WVTR (A) and WVP (B) of *it*-P3HB$_b$, *it-s*4-P3HB (M_n = 152 kg mol^{-1}, Đ = 1.22), and commodity plastics.

barrier properties of *it-s*4-P3HB (M_n = 152 kg mol^{-1}, Đ = 1.22) were investigated and compared to *it*-P3HB$_b$ as well as selected commodity plastics HDPE and LDPE. For instance, commercially available bacterial *it-(R)*-P3HB (Aldrich, M_w = 437 kDa) exhibits a low water vapor transmission rate (WVTR) of 0.08 ± 0.005 g h^{-1} m^{-2} and a water permeance (WVP) of 5.1 ± 0.14 (g h^{-1} s^{-1} Pa^{-1}) × 10^{12}. While one might anticipate that *it-s*4-P3HB would have inferior barrier properties compared to linear *it*-P3HB due to its lower degree of crystallinity, its star-like structured architecture could potentially modify these properties. Indeed, the measured values of WVTR and WVP for *it-s*4-P3HB are 0.03 ± 0.013 g h^{-1} m^{-2} and 2.6 ± 0.68 (g h^{-1} s^{-1} Pa^{-1}) × 10^{12}, respectively (Fig. 6), which showed comparable barrier properties to HDPE and LDPE (as judged by the WVP values) but superior to its linear *it-(R)*-P3HB counterpart. We postulate that the distinctive architecture of star-shaped P3HB, characterized by a compact structure and increased intramolecular entanglements among the polymer arms, leads to reduced free volume, creating more tortuous paths for gas diffusion and thus resulting in improved overall barrier properties.

Conclusions

In summary, we have synthesized four-arm star-shaped P3HBs encompassing stereo-perfect isotactic stereomicrostructures to stereo-defected iso-rich and syndio-rich stereomicrostructures, *it-s*4-P3HB (P_m > 0.99), *ir-s*4-P3HB (P_m = 0.91), and *sr-s*4-P3HB (P_r = 0.79), as well as their linear counterparts of comparable molar mass as controls. Comprehensive, comparative characterization studies revealed various degrees of impact of the P3HB architecture on thermal transitions, crystallization behavior, mechanical performance, rheological properties, and barrier properties. Notably, coupling the engineering of both stereomicrostructure and architecture has resulted in a synergistically enhanced impact on the overall material properties of P3HB.

From the stereomicrostructure engineering perspective, the incorporation of stereo-defects into the polymer chains limits the crystallization of the materials and reduces the spherulitic sizes up to more than two orders of magnitude, thereby improving mechanical properties. From the architecture perspective, having a higher ordered architecture, such as the

star-shaped P3HBs described herein, improves tensile strength, fracture strain, toughness, and melt processability, as compared to their linear counterparts. Notably, the branching in the star-P3HB facilitates a denser packing of polymer chains, thereby reducing the free volume within the material. In essence, a more tightly packed structure can hinder the movement of gas molecules and improve its barrier properties to both water transmittance rate and permeance relative to its linear counterpart.

In a broader context, this work advances architectural engineering approaches towards mono-material design for plastic products, demonstrating the potential of engineering macromolecular architectures as an additional design tool for mono-materials. In particular, coupling both stereomicrostructure and architectural engineering approaches provides a more powerful strategy to design plastics with vastly different, on-demand properties, all achievable without changing their chemical composition.

Author contributions

M. T. G.: investigation, data curation, writing – original draft, writing – review & editing, visualization, methodology, and validation. E. C. Q.: investigation, writing – review & editing, visualization, and methodology. F. S.: investigation and data curation. J. L. O.: investigation and data curation. S. X.: investigation. A. J. M.: resources, writing – review & editing, supervision, and project administration. E. Y.-X. C.: conceptualization, resources, writing – review & editing, supervision, project administration, and funding acquisition.

Conflicts of interest

M. T. G., E. C. Q. and E. Y.-X. C. declare the following competing financial interest(s): a provisional patent (63/565,866) has been filed by the Colorado State University Research Foundation on findings reported here. The rest of the authors declare no competing financial interests.

Data availability

The data supporting this article have been included as part of the SI. Supplementary information is available. See DOI: https://doi.org/10.1039/d5py00691k.

Acknowledgements

References

1 R. Geyer, J. R. Jambeck and K. L. Law, Production, Use, and Fate of All Plastics Ever Made, *Sci. Adv.*, 2017, **3**, e1700782.

2 P. G. C. N. T. Pilapitiya and A. S. Ratnayake, The World of Plastic Waste: A Review, *Cleaner Mater.*, 2024, **11**, 100220.

3 Y. Xiang, L. Jiang, Y. Zhou, Z. Luo, D. Zhi, J. Yang and S. S. Lam, Microplastics and Environmental Pollutants: Key Interaction and Toxicology in Aquatic and Soil Environments, *J. Hazard. Mater.*, 2022, **422**, 126843.

4 Y. Chae and Y. J. An, Current Research Trends on Plastic Pollution and Ecological Impacts on the Soil Ecosystem: A Review, *Environ. Pollut.*, 2018, **240**, 387–395.

5 L. Lebreton and A. Andrady, Future Scenarios of Global Plastic Waste Generation and Disposal, *Palgrave Commun.*, 2019, **5**, 1–11.

6 S. B. Borrelle, J. Ringma, K. L. Law, C. C. Monnahan, L. Lebreton, A. McGivern, E. Murphy, J. Jambeck, G. H. Leonard, M. A. Hilleary, M. Eriksen, H. P. Possingham, H. De Frond, L. R. Gerber, B. Polidoro, A. Tahir, M. Bernard, N. Mallos, M. Barnes and C. M. Rochman, Predicted Growth in Plastic Waste Exceeds Efforts to Mitigate Plastic Pollution, *Science*, 2020, **369**, 1515–1518.

7 A. L. Andrady and M. A. Neal, Applications and Societal Benefits of Plastics, *Philos. Trans. R. Soc., B*, 2009, **364**, 1977–1984.

8 C. Shi, L. T. Reilly, V. S. P. Kumar, M. W. Coile, S. R. Nicholson, L. J. Broadbelt, G. T. Beckham and E. Y.-X. Chen, Design Principles for Intrinsically Circular Polymers with Tunable Properties, *Chem*, 2021, **7**, 2896–2912.

9 G. Kwon, D. W. Cho, J. Park, A. Bhatnagar and H. Song, A Review of Plastic Pollution and Their Treatment Technology: A Circular Economy Platform by Thermochemical Pathway, *J. Chem. Eng.*, 2023, **464**, 142771.

10 T. H. Epps, L. T. J. Korley, T. Yan, K. L. Beers and T. M. Burt, Sustainability of Synthetic Plastics: Considerations in Materials Life-Cycle Management, *J. Am. Chem. Soc. Au*, 2022, **2**, 3–11.

11 A. Samir, F. H. Ashour, A. A. A. Hakim and M. Bassyouni, Recent Advances in Biodegradable Polymers for Sustainable Applications, *npj Mater. Degrad.*, 2022, **6**, 68.

12 N. Singh, O. A. Ogunseitan, M. H. Wong and Y. Tang, Sustainable Materials Alternative to Petrochemical Plastics Pollution: A Review Analysis, *Sustain. Horiz.*, 2022, **2**, 100016.

13 J. G. Rosenboom, R. Langer and G. Traverso, Bioplastics for a Circular Economy, *Nat. Rev. Mater.*, 2022, **7**, 117–137.

14 T. D. Moshood, G. Nawanir, F. Mahmud, F. Mohamad, M. H. Ahmad and A. AbdulGhani, Biodegradable Plastic Applications towards Sustainability: A Recent Innovations in the Green Product, *Clean. Eng. Technol.*, 2022, **6**, 100404.

15 R. Sehgal and R. Gupta, Polyhydroxyalkanoate and Its Efficient Production: An Eco-Friendly Approach towards Development, *3 Biotech.*, 2020, **10**, 549.

16 K. W. Meereboer, M. Misra and A. K. Mohanty, Review of Recent Advances in the Biodegradability of Polyhydroxyalkanoate (PHA) Bioplastics and Their Composites, *Green Chem.*, 2020, **22**, 5519–5558.

17 A. H. Westlie, E. C. Quinn, C. R. Parker and E. Y.-X. Chen, Synthetic Biodegradable Polyhydroxyalkanoates (PHAs): Recent Advances and Future Challenges, *Prog. Polym. Sci.*, 2022, **134**, 101608.

18 L. S. Dilkes-Hoffman, P. A. Lant, B. Laycock and S. Pratt, The Rate of Biodegradation of PHA Bioplastics in the Marine Environment: A Meta-Study, *Mar. Pollut. Bull.*, 2019, **142**, 15–24.

19 H.-M. Müller and D. Seebach, Poly(Hydroxyalkanoates): A Fifth Class of Physiologically Important Organic Biopolymers?, *Angew. Chem., Int. Ed. Engl.*, 1993, **32**, 477–502.

20 S. M. A. Muhammadi and S. Hameed, Bacterial Polyhydroxyalkanoates-Eco-Friendly next Generation Plastic: Production, Biocompatibility, Biodegradation, Physical Properties and Applications, *Green Chem. Lett. Rev.*, 2015, **8**, 56–77.

21 Z. Li, J. Yang and X. J. Loh, Polyhydroxyalkanoates: Opening Doors for a Sustainable Future, *NPG Asia Mater.*, 2016, **8**, e265.

22 K. Sudesh, H. Abe and Y. Doi, Synthesis, Structure and Properties of Polyhydroxyalkanoates: Biological Polyesters, *Prog. Polym. Sci.*, 2000, **25**, 1503–1555.

23 B. Laycock, P. Halley, S. Pratt, A. Werker and P. Lant, The Chemomechanical Properties of Microbial Polyhydroxyalkanoates, *Prog. Polym. Sci.*, 2013, **38**, 536–583.

24 A. Sangroniz, J. B. Zhu, X. Tang, A. Etxeberria, E. Y.-X. Chen and H. Sardon, Packaging Materials with Desired Mechanical and Barrier Properties and Full Chemical Recyclability, *Nat. Commun.*, 2019, **10**, 3559.

25 D. Tan, Y. Wang, Y. Tong and G. Q. Chen, Grand Challenges for Industrializing Polyhydroxyalkanoates (PHAs), *Trends Biotechnol.*, 2021, **39**, 953–963.

26 A. Anjum, M. Zuber, K. M. Zia, A. Noreen, M. N. Anjum and S. Tabasum, Microbial Production of Polyhydroxyalkanoates (PHAs) and Its Copolymers: A Review of Recent Advancements, *Int. J. Biol. Macromol.*, 2016, **89**, 161–174.

27 Y. Wang, J. Yin and G. Q. Chen, Polyhydroxyalkanoates, Challenges and Opportunities, *Curr. Opin. Biotechnol.*, 2014, **30**, 59–65.

28 A. Steinbüchel, Perspectives for Biotechnological Production and Utilization of Biopolymers: Metabolic Engineering of Polyhydroxyalkanoate Biosynthesis Pathways as a Successful Example, *Macromol. Biosci.*, 2001, **1**, 1–24.

29 R. W. Lenz and R. H. Marchessault, Bacterial Polyesters: Biosynthesis, Biodegradable Plastics and Biotechnology, *Biomacromolecules*, 2005, **6**, 1–8.

30 S. Inoue, Y. Tomoi, T. Tsuruta, J. Furukawa, T. L. Gresham, J. E. Jansen, F. W. Shaver and J. Amer, Organometallic-Catalyzed Polymerization of Propiolactone, *Die Makromol. Chem.*, 1961, **48**, 229–233.

31 N. Tanahashi and Y. Doi, Thermal Properties and Stereoregularity of Poly(3-Hydroxybutyrate) Prepared from Optically Active β-Butyrolactone with a Zinc-Based Catalyst, *Macromolecules*, 1991, **24**, 5732–5733.

32 D. E. Agostini, J. B. Lando and J. R. Shelton, Synthesis and Characterization of Poly-β-Hydroxybutyrate. I. Synthesis of Crystalline DL-Poly-β-Hydroxybutyrate from DL-β-Butyrolactone, *J. Polym. Sci.*, 1971, **9**, 2775–2787.

33 S. Bloembergen, D. A. Holden, T. L. Bluhm, G. K. Hamer and R. H. Marchessault, Stereoregularity in Synthetic 0-Hydroxybutyrate and /3-Hydroxyvalerate Homopolyesters, *Macromolecules*, 1989, **22**, 1656–1663.

34 N. Ajellal, G. Durieux, L. Delevoye, G. Tricot, C. Dujardin, C. M. Thomas and R. M. Gauvin, Polymerization of Racemic β-Butyrolactone Using Supported Catalysts: A Simple Access to Isotactic Polymers, *Chem. Commun.*, 2010, **46**, 1032–1034.

35 T. V. Mahrova, G. K. Fukin, A. V. Cherkasov, A. A. Trifonov, N. Ajellal and J. F. Carpentier, Yttrium Complexes Supported by Linked Bis(Amide) Ligand: Synthesis, Structure, and Catalytic Activity in the Ring-Opening Polymerization of Cyclic Esters, *Inorg. Chem.*, 2009, **48**, 4258–4266.

36 J. Bruckmoser, S. Pongratz, L. Stieglitz and B. Rieger, Highly Isoselective Ring-Opening Polymerization of Rac-β-Butyrolactone: Access to Synthetic Poly(3-Hydroxybutyrate) with Polyolefin-like Material Properties, *J. Am. Chem. Soc.*, 2023, **145**, 11494–11498.

37 M. Zintl, F. Molnar, T. Urban, V. Bernhart, P. Preishuber-Pflügl and B. Rieger, Variably Isotactic Poly(Hydroxybutyrate) from Racemic β-Butyrolactone: Microstructure Control by Achiral Chromium(III) Salophen Complexes, *Angew. Chem., Int. Ed.*, 2008, **47**, 3458–3460.

38 A. Le Borgne and N. Spassky, Stereoelective Polymerization of β-Butyrolactone, *Polymer*, 1989, **30**, 2312–2319.

39 Y. Hori and T. Hagiwara, Ring-Opening Polymerisation of β-Butyrolactone Catalysed by Distannoxane Complexes: Study of the Mechanism, *Int. J. Biol. Macromol.*, 1999, **25**, 237–245.

40 H. Y. Huang, W. Xiong, Y. T. Huang, K. Li, Z. Cai and J. B. Zhu, Spiro-Salen Catalysts Enable the Chemical Synthesis of Stereoregular Polyhydroxyalkanoates, *Nat. Catal.*, 2023, **6**, 720–728.

41 M. Arcana, O. Giani-Beaune, F. Schue, W. Amass and A. Amass, Structure and Morphology of Poly(b-Hydroxy-Butyrate) Synthesized by Ring-Opening Polymerization of

Racemic (R,S)-b-Butyrolactone with Distannoxane Derivatives, *Polym. Int.*, 2000, **49**, 1348–1355.

42 Y. Hori, M. Suzuki, A. Yamaguchi and T. Nishishita, Ring-Opening Polymerization of Optically Active. β-Butyrolactone Using Distannoxane Catalysts: Synthesis of High Molecular Weight Poly(3-Hydroxybutyrate), *Macromolecules*, 1993, **26**, 5533–5534.

43 S. Hörl, I. Chiorescu, J. Bruckmoser, J. Futter and B. Rieger, Influence of Ligand Design and Non-Covalent Interactions on the Isoselective Ring-Opening Polymerization of Rac-β-Butyrolactone Using Salan and Salalen Rare-Earth Metal Catalysts, *Angew. Chem., Int. Ed.*, 2025, **64**, e202504513.

44 M. S. Young, A. M. LaPointe, S. N. MacMillan and G. W. Coates, Highly Enantioselective Polymerization of β-Butyrolactone by a Bimetallic Magnesium Catalyst: An Interdependent Relationship Between Favored and Unfavored Enantiomers, *J. Am. Chem. Soc.*, 2024, **146**, 18032–18040.

45 X. Tang and E. Y.-X. Chen, Chemical Synthesis of Perfectly Isotactic and High Melting Bacterial Poly(3-Hydroxybutyrate) from Bio-Sourced Racemic Cyclic Diolide, *Nat. Commun.*, 2018, **9**, 1–11.

46 X. Tang, A. H. Westlie, L. Caporaso, L. Cavallo, L. Falivene and E. Y.-X. Chen, Biodegradable Polyhydroxyalkanoates by Stereoselective Copolymerization of Racemic Diolides: Stereocontrol and Polyolefin-Like Properties, *Angew. Chem., Int. Ed.*, 2020, **59**, 7881–7890.

47 A. H. Westlie, S. A. Hesse, X. Tang, E. C. Quinn, C. R. Parker, C. J. Takacs, C. J. Tassone and E. Y.-X. Chen, All-Polyhydroxyalkanoate Triblock Copolymers via a Stereoselective-Chemocatalytic Route, *ACS Macro. Lett.*, 2023, **12**, 619–625.

48 X. Tang, C. Shi, Z. Zhang and E. Y.-X. Chen, Toughening Biodegradable Isotactic Poly(3-Hydroxybutyrate) via Stereoselective Copolymerization of a Diolide and Lactones, *Macromolecules*, 2021, **54**, 9401–9409.

49 X. Tang, C. Shi, Z. Zhang and E. Y.-X. Chen, Crystalline Aliphatic Polyesters from Eight-Membered Cyclic (Di) Esters, *J. Polym. Sci.*, 2022, **60**, 3478–3488.

50 C. G. Jaffredo, J. F. Carpentier and S. M. Guillaume, Poly (Hydroxyalkanoate) Block or Random Copolymers of β-Butyrolactone and Benzyl β-Malolactone: A Matter of Catalytic Tuning, *Macromolecules*, 2013, **46**, 6765–6776.

51 N. Ajellal, C. M. Thomas and J. F. Carpentier, Functional Syndiotactic Poly(β-Hydroxyalkanoate)s via Stereoselective Ring-Opening Copolymerization of Rac-β-Butyrolactone and Rac-Allyl-β-Butyrolactone, *J. Polym. Sci., Part A:Polym. Chem.*, 2009, **47**, 3177–3189.

52 E. C. Quinn, A. H. Westlie, A. Sangroniz, M. R. Caputo, S. Xu, Z. Zhang, M. Urgun-Demirtas, A. J. Müller and E. Y.-X. Chen, Installing Controlled Stereo-Defects Yields Semicrystalline and Biodegradable Poly(3-Hydroxybutyrate) with High Toughness and Optical Clarity, *J. Am. Chem. Soc.*, 2022, **45**, 5795–5802.

53 Z. Zhang, E. C. Quinn, J. L. Olmedo-Martínez, M. R. Caputo, K. A. Franklin, A. J. Müller and E. Y.-X. Chen, Toughening Brittle Bio-P3HB with Synthetic P3HB of Engineered Stereomicrostructures, *Angew. Chem., Int. Ed.*, 2023, **62**, e202311264.

54 X. Tang, A. H. Westlie, E. M. Watson and E. Y.-X. Chen, Stereosequenced Crystalline Polyhydroxyalkanoates from Diastereomeric Monomer Mixtures, *Science*, 2019, **366**, 754–758.

55 Z. Zhang, C. Shi, M. Scoti, X. Tang and E. Y.-X. Chen, Alternating Isotactic Polyhydroxyalkanoates via Site- and Stereoselective Polymerization of Unsymmetrical Diolides, *J. Am. Chem. Soc.*, 2022, **144**, 20016–20024.

56 L. Zhou, Z. Zhang, C. Shi, M. Scoti, D. K. Barange, R. R. Gowda and E. Y.-X. Chen, Chemically Circular, Mechanically Tough, and Melt-Processable Polyhydroxyalkanoates., *Science*, 2023, **380**, 64–69.

57 E. C. Quinn, K. M. Knauer, G. T. Beckham and E. Y.-X. Chen, Mono-Material Product Design with Bio-Based, Circular, and Biodegradable Polymers, *One Earth*, 2023, **6**, 582–586.

58 T. I. Butler and B. A. Morris, *Multilayer Flexible Packaging*, Elsevier, 2016.

59 T. Anukiruthika, P. Sethupathy, A. Wilson, K. Kashampur, J. A. Moses and C. Anandharamakrishnan, Multilayer Packaging: Advances in Preparation Techniques and Emerging Food Applications, *Compr. Rev. Food Sci. Food Saf.*, 2020, **19**, 1156–1186.

60 J. M. Ren, T. G. McKenzie, Q. Fu, E. H. H. Wong, J. Xu, Z. An, S. Shanmugam, T. P. Davis, C. Boyer and G. G. Qiao, Star Polymers, *Chem. Rev.*, 2016, **116**, 6743–6836.

61 S. Liffland and M. A. Hillmyer, Enhanced Mechanical Properties of Aliphatic Polyester Thermoplastic Elastomers through Star Block Architectures, *Macromolecules*, 2021, **54**, 9327–9340.

62 J. Liu, M. Jia, Y. Gnanou and X. Feng, Heat-Resistant CO2-Based Polycarbonate Thermoplastics, *Macromolecules*, 2024, **57**, 5380–5388.

63 W. Wu, W. Wang and J. Li, Star Polymers: Advances in Biomedical Applications, *Prog. Polym. Sci.*, 2015, **46**, 55–85.

64 R. A. Patil, N. H. Aloorkar, A. S. Kulkarni and D. J. Ingale, Star Polymers: An Overview, *Int. J. Pharm. Nanotechnol. Res.*, 2012, **5**, 1675–1684.

65 G. Lapienis, Star-Shaped Polymers Having PEO Arms, *Prog. Polym. Sci.*, 2009, **34**, 852–892.

66 A. Chremos and J. F. Douglas, Influence of Branching on the Configurational and Dynamical Properties of Entangled Polymer Melts, *Polymers*, 2019, **11**, 1045.

67 A. Giuntoli, A. Chremos and J. F. Douglas, Influence of Polymer Topology on Crystallization in Thin Films, *J. Chem. Phys.*, 2020, **152**, 044501.

68 J. Roovers, *Star and Hyperbranched Polymers*, 1998.

69 D. E. Dunstan, The Viscosity-Radius Relationship for Concentrated Polymer Solutions, *Sci. Rep.*, 2019, **9**, 1–9.

70 A. B. Burns and R. A. Register, Mechanical Properties of Star Block Polymer Thermoplastic Elastomers with Glassy and Crystalline End Blocks, *Macromolecules*, 2016, **49**, 9521–9530.

71 S. Liffland, M. Kumler and M. A. Hillmyer, High Performance Star Block Aliphatic Polyester Thermoplastic Elastomers Using PDLA-b-PLLA Stereoblock Hard Domains, *ACS Macro Lett.*, 2023, 1331–1338.

72 D. J. A. Cameron and M. P. Shaver, Aliphatic Polyester Polymer Stars: Synthesis, Properties and Applications in Biomedicine and Nanotechnology, *Chem. Soc. Rev.*, 2011, **40**, 1761–1776.

73 T. Ebrahimi, S. G. Hatzikiriakos and P. Mehrkhodavandi, Synthesis and Rheological Characterization of Star-Shaped and Linear Poly(Hydroxybutyrate), *Macromolecules*, 2015, **48**, 6672–6681.

74 R. Omar, M. Shaik, C. Griggs, J. D. Jensen, R. Boyd, N. Oncel, D. C. Webster and G. Du, Star-Shaped Poly (Hydroxybutyrate)s from Bio-Based Polyol Cores via Zinc Catalyzed Ring-Opening Polymerization of β-Butyrolactone, *Eur. Polym. J.*, 2021, **160**, 110756.

75 R. Anwander, O. Runte, J. Eppinger, G. Gerstberger, E. Herdtweck and M. Spiegler, Synthesis and Structural Characterisation of Rare-Earth Bis(Dimethylsilyl)Amides and Their Surface Organometallic Chemistry on Mesoporous MCM-41, *J. Chem. Soc., Dalton Trans.*, 1998, **11**, 847–858.

76 Q. Liu, C. Meermann, H. W. Görlitzer, O. Runte, E. Herdtweck, P. Sirsch, K. W. Törnroos and R. Anwander, Cationic Rare-Earth Metal SALEN Complexes, *Dalton Trans.*, 2008, **44**, 6170–6178.

77 X. L. Li, R. W. Clarke, J. Y. Jiang, T. Q. Xu and E. Y.-X. Chen, A Circular Polyester Platform Based on Simple Gem-Disubstituted Valerolactones, *Nat. Chem.*, 2023, **15**, 278–285.

78 A. Sangroniz, L. Sangroniz, N. Aranburu, M. Fernández, A. Santamaria, M. Iriarte and A. Etxeberria, Blends of Biodegradable Poly(Butylene Adipate-Co-Terephthalate) with Poly(Hydroxi Amino Ether) for Packaging Applications: Miscibility, Rheology and Transport Properties, *Eur. Polym. J.*, 2018, **105**, 348–358.

79 American Society for Testing and Materials, ASTM E96/ E96M-16 Standard Test Methods for Water Vapor Transmission of Materials, in *Annual Book of American Standard Testing Methods*, 2016.

80 Z. Zhang, E. C. Quinn, J. K. Kenny, A. Grigoropoulos, J. S. DesVeaux, T. Chen, L. Zhou, T. Xu, G. T. Beckham and E. Y.-X. Chen, Stereomicrostructure-Regulated Biodegradable Adhesives, *Science*, 2025, **387**, 297–303.

81 A. J. Müller, Z. H. Hernandez, M. L. Arnal and J. J. Sanchez, Successive Self-Nucleation/Annealing (SSA): A Novel Technique to Study Molecular Segregation during Crystallization, *Polym. Bull.*, 1997, **39**, 465–472.

82 R. A. Pérez-Camargo, D. Cavallo and A. J. Müller, Recent Applications of the Successive Self-Nucleation and Annealing Thermal Fractionation Technique, *Front. Soft Matter*, 2022, **2**, 1003500.

83 A. J. Müller, R. M. Michell, R. A. Pérez and A. T. Lorenzo, Successive Self-Nucleation and Annealing (SSA): Correct Design of Thermal Protocol and Applications, *Eur. Polym. J.*, 2015, **65**, 132–154.

84 M. L. Arnal, V. Balsamo, G. Ronca, A. Sánchez, A. J. Müller, E. Cañizales and C. Urbina De Navarro, Applications OF Successive Self-Nucleation and Annealing (SSA) to Polymer Characterization, *J. Therm. Anal. Calorim.*, 2000, **59**, 451–470.

85 L. Sangroniz, Y. J. Jang, M. A. Hillmyer and A. J. Müller, The Role of Intermolecular Interactions on Melt Memory and Thermal Fractionation of Semicrystalline Polymers, *J. Chem. Phys.*, 2022, **156**, 144902.

86 M. R. Caputo, X. Tang, A. H. Westlie, H. Sardon, E. Y.-X. Chen and A. J. Müller, Effect of Chain Stereoconfiguration on Poly(3-Hydroxybutyrate) Crystallization Kinetics, *Biomacromolecules*, 2022, **23**, 3847–3859.

87 J. Xu, H. Ye, S. Zhang and B. Guo, Organization of Twisting Lamellar Crystals in Birefringent Banded Polymer Spherulites: A Mini-Review, *Crystals*, 2017, **7**, 241.

88 H. D. Keith and F. J. Padden, Banding in Polyethylene and Other Spherulites, *Macromolecules*, 1996, **29**, 7776–7786.

89 A. J. Lovinger, Twisted Crystals and the Origin of Banding in Spherulites of Semicrystalline Polymers, *Macromolecules*, 2020, **53**, 741–745.

90 X. Hou, W. Sun, Z. Liu, S. Liu, J. C. C. Yeo, X. Lu and C. He, Tailoring Crystalline Morphology via Entropy-Driven Miscibility: Toward Ultratough, Biodegradable, and Durable Polyhydroxybutyrate, *Macromolecules*, 2022, **55**, 5527–5534.

91 M. Eesaee, P. Ghassemi, D. D. Nguyen, S. Thomas, S. Elkoun and P. Nguyen-Tri, Morphology and Crystallization Behaviour of Polyhydroxyalkanoates-Based Blends and Composites: A Review, *Biochem. Eng. J.*, 2022, **187**, 108588.